Validation of MRI-based 3D digital atlas registration with histological and autoradiographic volumes: An anatomofunctional transgenic mouse brain imaging study

J. Lebenberg [a], A.-S. Hérard [a], A. Dubois [b], J. Dauguet [a], V. Frouin [c], M. Dhenain [a], P. Hantraye [a], T. Delzescaux [a,*]

[a] CEA-DSV-I2BM-MIRCen, CNRS URA2210, F-92265 Fontenay aux Roses Cedex, France
[b] CEA-DSV-I2BM-SHFJ, INSERM U803, F-91401 Orsay Cedex, France
[c] CEA-DSV-I2BM-Neurospin, F-91191 Gif sur Yvette Cedex, France

ABSTRACT

Murine models are commonly used in neuroscience to improve our knowledge of disease processes and to test drug effects. To accurately study neuroanatomy and brain function in small animals, histological staining and *ex vivo* autoradiography remain the gold standards to date. These analyses are classically performed by manually tracing regions of interest, which is time-consuming. For this reason, only a few 2D tissue sections are usually processed, resulting in a loss of information. We therefore proposed to match a 3D digital atlas with previously 3D-reconstructed *post mortem* data to automatically evaluate morphology and function in mouse brain structures. We used a freely available MRI-based 3D digital atlas derived from C57Bl/6J mouse brain scans (9.4 T). The histological and autoradiographic volumes used were obtained from a preliminary study in $APP_{SL}/PS1_{M146L}$ transgenic mice, models of Alzheimer's disease, and their control littermates ($PS1_{M146L}$). We first deformed the original 3D MR images to match our experimental volumes. We then applied deformation parameters to warp the 3D digital atlas to match the data to be studied. The reliability of our method was qualitatively and quantitatively assessed by comparing atlas-based and manual segmentations in 3D. Our approach yields faster and more robust results than standard methods in the investigation of *post mortem* mouse data sets at the level of brain structures. It also constitutes an original method for the validation of an MRI-based atlas using histology and autoradiography as anatomical and functional references, respectively.

© 2010 Elsevier Inc. All rights reserved.

Introduction

Murine models are commonly used to improve our understanding of the pathophysiology of human diseases and to determine the effects of drugs. In the study of neurodegenerative diseases such as Alzheimer's disease (AD), images of the brain are acquired and analyzed to evaluate the anatomofunctional changes involved in the evolution of the neurological disorder. However, rodent brain analysis by *in vivo* imaging remains a challenging task because of the limited resolution of scans (100–500 μm for positron emission tomography (PET) and magnetic resonance imaging (MRI)) due to the size of the brain and the short acquisition time imposed by studies in live animals. More information can be obtained from MR images acquired *ex vivo* (~50 μm isotropic resolution for MR image presented in Ma et al. (2005)). Nevertheless, for a microscopic and accurate description of neuroanatomy and brain function, the respective gold standards

remain histological staining and *ex vivo* autoradiography (Wong et al., 2002; Valla et al., 2006). A major drawback of these techniques is that the data yielded by such tissue sections, which we refer to here as "*post mortem* data" is limited to two dimensions. The 3D spatial coherence of the structure is generally lost, and analysis is restricted to a limited number of sections. *Post mortem* data are traditionally analyzed by manually outlining regions of interest (ROI), guided by a 2D atlas (Swanson, 1998; Paxinos and Franklin, 2001). In addition to the need for expertise, this task is labor-intensive, time-consuming (~3 min was required to accurately segment one ROI on one slice), and subject to intra/interoperator bias. Moreover, the preparation of sections is a tedious process, and the sections presented in the atlas are not equidistant throughout the organ, adding to the difficulty in identifying the structures or levels involved. A considerable proportion of the information provided by histological studies in the *post mortem* rodent brain thus remains unexploited. To overcome these limitations, we used numerous serial sections to obtain a spatially coherent 3D reconstruction of the brain that could be easily and automatically analyzed.

At this point, two analytical strategies were open to us: ROI analysis using segmentation determined by 1) a voxel-wise approach,

* Corresponding author. MIRCen-LMN-CNRS-URA2210, CEA-DSV-I2BM, 18 route du Panorama, F-92265 Fontenay Aux Roses Cedex, France. Fax: +33 1 46 54 84 51.
E-mail address: thierry.delzescaux@cea.fr (T. Delzescaux).

2) a 3D digital atlas. The voxel-wise approach permits statistical comparisons between groups at the single-voxel scale and can be achieved with dedicated tools such as the Statistical Parametric Mapping (SPM) software (Wellcome Department of Imaging Neuroscience, London, UK). Initially developed for clinical studies, few studies on rodent models have been performed with SPM (Nguyen et al., 2004; Dubois et al., 2008b). The major constraints of this approach are the requirement for an adequate database (number of subjects) and the need to deform data within a common spatial reference frame. Contrary to the voxel-wise approach, atlas-based analysis has several important advantages. For instance, it does not require a minimum number of subjects, and the study is based on atlas deformation in the frame of reference of the data, preserving their original geometry. There are certain prerequisites to atlas use: the atlas must be aligned with the data and the segmentation yielded must be validated by comparison with a reference segmentation that could be either an already validated segmentation such as a probabilistic atlas or, as in our case, a segmentation based on manual delineation carried out by a neuroanatomist.

Whereas some digital rodent atlases have been created for teaching purposes (cf., Dhenain et al. (2001) and BrainNavigator, the interactive atlas and 3D Brain software at http://www.brainnav.com/home/) or for data sharing (Boline et al., 2008), others are now used to analyze data. Some of these are created from digital 2D atlas diagrams (Hjornevik et al., 2007; Purger et al., 2009). However, their use is contested because of the low 3D spatial coherence of the reconstructed volume (Yelnik et al., 2007). The number of MRI-based atlases being created is constantly increasing (Dorr et al., 2008), and whereas the first atlases were manually delineated (Mackenzie-Graham et al., 2004; Bock et al., 2006), several teams are currently developing algorithms for the semiautomated segmentation of the mouse brain using MRI (Ali et al., 2005; Ma et al., 2005; Sharief et al., 2008; Scheenstra et al., 2009).

As some of these MRI-based 3D digital rodent brain atlases have been made available on the Internet (Mackenzie-Graham et al., 2004; Johnson et al., 2007) and more recently Ma et al. (2008), we proposed to match one of them to our *post mortem* data to fully and automatically segment cerebral structures in *post mortem* data sets. Such atlases have already been used in several studies to analyze *in vivo* MRI volumes (Bock et al., 2006; Ma et al., 2008; Maheswaran et al., 2009a) or *ex vivo* MR images (Ma et al., 2005; Badea et al., 2009). Nevertheless, to our knowledge, this approach has not so far been used to study 3-dimensionally reconstructed (3D-reconstructed) *post mortem* data (i.e., histological and autoradiographic volumes). This article thus provides a strategy to register an MRI-based 3D digital atlas to *post mortem* mouse brain volumes. Its reliability was assessed qualitatively and quantitatively by comparing atlas-based segmentation with manual segmentation, performed on histological volumes. The method was developed in the context of a preliminary study of $APP_{SL}/PS1_{M146L}$ transgenic mice, models of Alzheimer's disease (AD), and their control littermates ($PS1_{M146L}$). It led to the determination of morphometric and functional parameters that were compared with results previously described in the literature.

Materials and methods

Biological data

Animals

Our method was applied to four $APP_{SL}/PS1_{M146L}$ (64 ± 1 weeks old) and three $PS1_{M146L}$ mice (65 ± 2 weeks old), with a C57Bl/6 genetic background. The $APP_{SL}/PS1_{M146L}$ transgenic strain models Alzheimer's disease by expressing the gene encoding the mutated human amyloid precursor protein (APP) under the control of the Thy-1 promoter and harbors three familial mutations: the Swedish K670M/N671L and London V717I mutations and the mutated presenilin 1 gene (PS1 with the M146L mutation). The incremental expression of mutated PS1 accelerates amyloid deposition (Blanchard et al., 2003). $PS1_{M146L}$ littermates, being amyloid-free, were used as controls for $APP_{SL}/PS1_{M146L}$ mice (Delatour et al., 2006). All procedures were carried out in accordance with the recommendations of the EEC (directive 86/609/EEC) and the French National Committee (decree 87/848) for the use of laboratory animals.

Data acquisition

[^{14}C]-2-deoxyglucose was injected *in vivo* (16.5 µCi/100 g body weight; Perkin Elmer, Boston, MA, USA) to evaluate cerebral glucose uptake by quantitative autoradiography. Additional details of deoxyglucose experiments are described in Herard et al. (2005) except that, in our study, animals were awake with no stimulation. Glucose metabolism was measured only in the right hemisphere, which was extracted following euthanasia for *ex situ* analysis and cut into 20-µm-thick serial coronal sections on a CM3050S cryostat (Leica, Rueil-Malmaison, France). The olfactory bulb and cerebellum were excluded. Every fourth serial section was mounted on a Superfrost glass slide and exposed to autoradiographic film (Kodak Biomax MR), with radioactive [^{14}C] standards (146C; American Radiochemical Company, St. Louis, MO). The same sections were next processed for Nissl staining to obtain anatomical information. Images from the brain surface, corresponding to sections subsequently processed, were recorded before sectioning using a digital camera (Canon Powershot G5 Pro 5 Mo pixel) with an in-plane resolution of 27×27 µm^2.

3D-reconstructed multimodal post mortem data

Block-face photographs were stacked and brain tissue was automatically segmented using a histogram analysis method. As these images were taken prior to sectioning at the exact same position section after section, the imaged brain was still attached to the block, and the resulting stack of photographs was therefore intrinsically spatially coherent. No section-to-section registration was required to reconstruct the block-face volume. The final block-face volume used was thus around a $350 \times 308 \times 120$ array with a resolution of $0.027 \times 0.027 \times 0.080$ mm^3. Autoradiographs, with [^{14}C] standards, and histological sections were digitized as 8-bit grayscale images using a flatbed scanner (ImageScanner; GE Healthcare Europe, Orsay, France) with a 1200 dpi in-plane resolution (pixel size 21×21 µm^2). As described in Dubois et al. (2008a), these *post mortem* images were stacked using BrainRAT, a new add-on of BrainVISA (free software, http://brainvisa.info/). Each slice of the stacked histological volume was first rigidly aligned with the corresponding block-face photograph. Each slice of the stacked autoradiographic volume was thereafter rigidly coaligned with its histological counterpart. The Block-Matching method, described in Ourselin et al. (2001), was used for intervolume registration (2D images registration). Final histological and autoradiographic volumes were in a $479 \times 420 \times 120$ array with a resolution of $0.021 \times 0.021 \times 0.080$ mm^3. For each animal, we obtained three spatially coherent 3D-reconstructed volumes with the same frame of reference (cf., Fig. 1). To measure glucose uptake, the gray level intensities of the autoradiographic volumes were calibrated using the co-exposed [^{14}C] standards and converted into activity values (nCi/g). Corrective coefficients were applied to normalize brain activity so as to allow comparison between strains (Valla et al., 2006).

MRI-based 3D digital mouse brain atlas

The MRI-based 3D digital atlas used for our study was downloaded from the Website of the Center for *In vivo* Microscopy (http://www.civm.duhs.duke.edu/); it is currently available at the Biomedical Informatics Research Network (BIRN) Data Repository (BDR) (https://bdr-portal.nbirn.net/). This atlas was derived from T1 and T2-weighted 3D MR images (9.4 T) of six young adult (9–12 weeks) C57Bl/6J mice (same genetic background as our animals). To enhance image quality, and preserve *in vivo* geometry, MR images were acquired *in situ*, i.e., within the cranial vault, after active staining of the brain (Johnson et al., 2007; Badea et al., 2007; Dorr et al., 2008). The isotropic scan resolutions
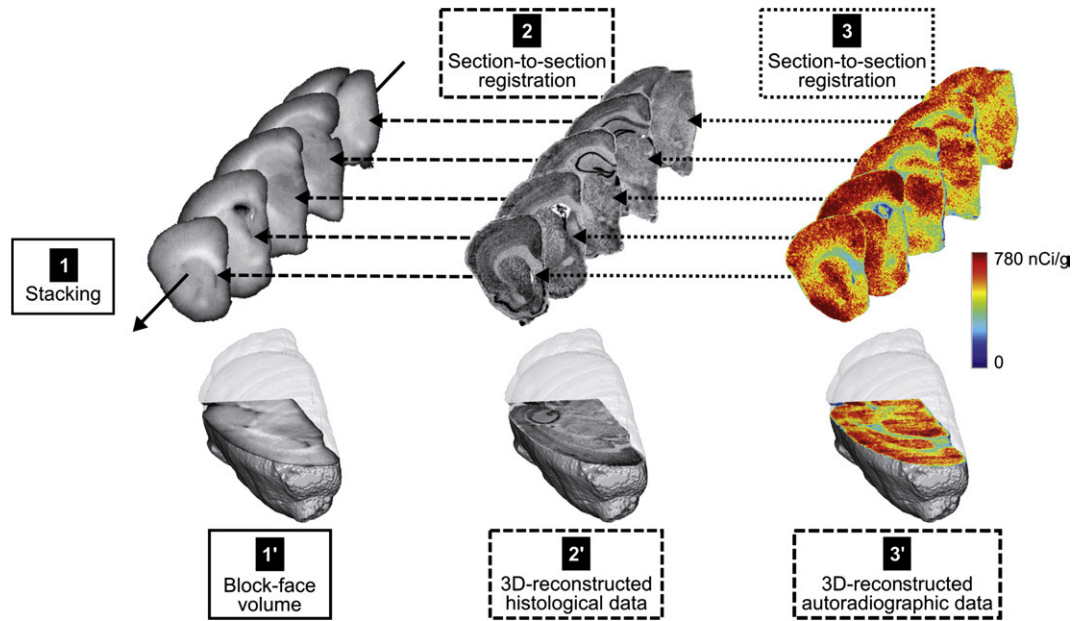
Fig. 1. 3D reconstruction of *post mortem* data. Photographs were stacked (1). As brain pictures were recorded before cutting, block-face volume (1′) was de facto spatially coherent. Digitized individual autoradiographic and histological sections were stacked with BrainRAT (Brain Reconstruction and Analysis Toolbox of BrainVISA). Each slice of the stacked histological volume was then rigidly registered to the corresponding block-face photograph (2) to create a 3D-reconstructed histological volume (2′) spatially coherent with the block-face volume. Each slice of the stacked autoradiographic volume was thereafter rigidly registered to the corresponding registered histological section (3). Autoradiographic data (3′) were thus spatially coherent with the first two volumes created. The Block-Matching method was used for these intervolume registrations.

were 21.5 μm (T1) and 43 μm (T2) using $512 \times 512 \times 1024$ and $256 \times 256 \times 512$ arrays, respectively. Thirty-three anatomical structures were segmented as described in Sharief et al. (2008).

MRI-based atlas and post mortem data registration strategy

To accurately analyze our experimental data, we chose to deform the atlas in the coordinate space of each experimental sample using the registration techniques detailed below. To optimize the process, we first registered T1-weighted MRI to *post mortem* data and then applied the estimated transformation to the digital atlas. We automatically reoriented the MRI and atlas volumes as described in Prima et al. (2002) to realign the interhemispheric plane with our referential axes. The hemisphere to be studied was thus automatically extracted. We then interactively cropped the MRI to select (and preserve) the part of the hemisphere to be registered (in our case, the cerebellum and olfactory bulb were excluded). The atlas volume was automatically cropped using the parameters determined previously (cf., dashed rectangle shown as step 0 in Fig. 2).

Our registration strategy aimed to compensate for volumetric differences and variability between mouse brains used for the atlas and mouse brains of our study. To overcome these variations, several teams have already proposed a strategy that consists of gradually increasing the number of degrees of freedom DOF (Bock et al., 2006; Badea et al., 2007; Dauguet et al., 2007; Ma et al., 2008; Li et al., 2009; Maheswaran et al., 2009a). Inspired by their work, we formulated a strategy to first register images globally, and then locally. It was defined according to the following steps:

1. A global rigid transformation was first estimated for each voxel of the T1-weighted MR image. Rotation and translation parameters were optimized using mutual information MI (Maes et al., 1997; Viola and Wells, 1997) as a similarity criterion.
2. An affine deformation initialized with previously computed parameters was then calculated with the Block-Matching registration technique (Ourselin et al., 2001) [volumes registration (3D)

optimized with the correlation coefficient (CC)]. A pyramidal approach speeded up the registration process and overcame problems with local minima.
3. Finally, to locally enhance MRI and *post mortem* data registration, we deformed this image using a nonlinear transformation initialized with the previously estimated transformation. To obtain a flexible but smooth registration of the different volumes, we chose an elastic transformation, the free form deformation (FFD), based on cubic *B*-spline transformation and using MI as a similarity criterion (Rueckert et al., 1999; Mattes et al., 2003). Setting regularly spaced $10 \times 10 \times 10$ control points throughout the volume, this deformation optimized 3×10^3 DOF.

These mathematical functions were all implemented in C++ using in house developed software. BrainVISA pipelines were developed in python to chain registration steps without operator intervention.

As the *post mortem* data were spatially coherent and had the same geometry, the final estimated transformation allowed the application of the registered atlas to any volume.

Reconstructions in 3D of our *post mortem* data were based on registration with the block-face volume, which was intrinsically spatially coherent. With its higher spatial coherence with respect to other modalities and its morphological similarity to MRI, the 3D photographic volume was first chosen as the reference image for the registration process. This approach has been taken previously by Yelnik et al. (2007) using a linear transformation and by Dauguet et al. (2007) using a nonlinear transformation. MR images have also previously been registered to 3D-reconstructed autoradiographic (Malandain et al., 2004) and histological data (Schormann et al., 1995; Chakravarty et al., 2006; Li et al., 2009). Similarly, we used our 3-step approach to register MRI data to the autoradiographic and histological volumes, to determine the reference volume (photographic, autoradiographic, or histological) that would result in the most suitable registration for reliable anatomofunctional analysis. In addition, we carried out supplementary tests, registering the MRI to
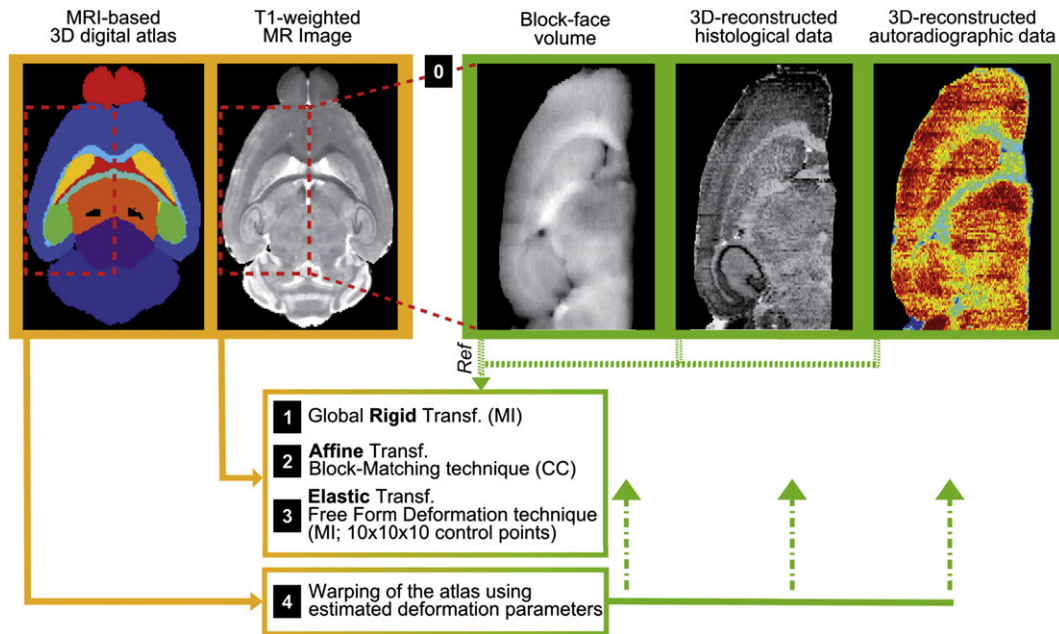
Fig. 2. MRI-based atlas and *post mortem* data registration strategy. The registration strategy was a three-step approach: (1) a global rigid transformation optimized with the mutual information (MI) was estimated on T1-weighted MR images cropped to obtain a brain volume similar to *post mortem* data (0); (2) an affine deformation initialized with previously computed parameters was calculated with the Block-Matching registration technique (optimization based on correlation coefficient (CC)); (3) a free form deformation initialized with the previous transformation and using MI as a similarity criterion to optimize 3 DOF for each control point was estimated to enhance data registration. The three spatially coherent *post mortem* volumes were tested as reference images for each step. Deformation parameters were then used to warp the 3D digital atlas to the *post mortem* geometry (4).

each of the three *post mortem* volumes to determine the optimal combination of reference images for each step.

Fig. 2 summarizes this proposed registration strategy.

Evaluation of registration

Registration accuracy was qualitatively and quantitatively evaluated at each step of the process. The qualitative evaluation consisted of a visual inspection of the superimposition of the inner and outer contours of the T1-weighted MR image (extracted using a Deriche Filter (Deriche, 1987)) registered on *post mortem* data. This evaluation was realized for the entire data set.

As a second step, to quantitatively evaluate our registration strategy, the concordance between atlas-based and manually delineated ROIs was measured with overlapping criteria. The hippocampus, cortex, and striatum, as well as the corpus callosum and substantia nigra, were thus manually delineated within the histological volume of one APP/PS1 and one PS1 mouse brain respectively by a neuroanatomist. Considering the expert needs ~3 min to accurately manually delineate an ROI on one slice, one hippocampus (on one hemisphere) was segmented in 3 hours. These ROIs were chosen because of their variation in terms of location and size: the cortex is a large paired structure that extends over the surface of the brain, up to the olfactory bulb. The hippocampus and striatum are also paired but slightly smaller. Both subcortical, the hippocampus is a complex region mainly localized in the posterior part of the brain, whereas the striatum has a simpler shape and is present in the anterior part of the brain. The striatum was not directly defined as an ROI in the atlas. We thus postprocessed the atlas-based segmentation to create the striatum by the fusion of the nucleus accumbens and caudate putamen ROIs. The corpus callosum is an unpaired very thin structure stuck between the cerebral cortex and the ventricles. The external capsule was included in the manual segmentation of the corpus callosum. Finally, the substantia nigra is a tiny and deep subthalamic structure, close to the posterior part of the midbrain.

We first computed the difference in volume (Δ_V) and the Dice coefficient (κ) defined in Eqs. (1) and (2), respectively.

$$\Delta_V = 2 \times \frac{|V_A - V_M|}{V_A + V_M} \tag{1}$$

$$\kappa = 2 \times \frac{V_A \cap V_M}{V_A + V_M} \tag{2}$$

where V_A and V_M are the volumes of the atlas-based and manual segmentation, respectively. The volume difference provides a good volumetric comparison of the two types of segmentation. The Dice coefficient, initially proposed by Dice (1945), quantifies segmentation superimposition in space from 0 to 1. Knowing that 1 corresponds to a perfect overlap, a Dice coefficient greater than 0.7 is considered in the literature to indicate a good level of concordance between the two types of segmentation (Zijdenbos et al., 1994).

To quantify the accuracy of the atlas and its efficacy in properly segmenting voxels, the sensitivity (Se) was also computed using Eq. (3).

$$Se = \frac{V_A \cap V_M}{V_M} \tag{3}$$

As mentioned previously, all *post mortem* data were spatially coherent. Manual segmentations performed on histological volumes could be applied on autoradiographic volumes and thus enable to measure a mean activity per ROI ($\mu_{act(M)}$). Similarly, registered atlas could provide a mean activity ($\mu_{act(A)}$). So, in addition to the computation of these volumetric criteria, we compared mean activity in the ROIs using both types of segmentation within the autoradiographic volume. Using Eq. (4), variation coefficients (δ_μ) were

computed for each structure to estimate atlas segmentation error in comparison with measurements using manual segmentation.

$$\delta_\mu = \frac{|\mu_{act(A)} - \mu_{act(M)}|}{\mu_{act(M)}} \tag{4}$$

Atlas-based segmentation of anatomofunctional data sets

Our methodology was applied to the entire data set (three control and four AD mice) to obtain anatomofunctional parameters using anatomical volumes (block-face or histological) and functional volume (autoradiographic), respectively. In addition to the hippocampus, cortex, corpus callosum, substantia nigra, and striatum, other ROIs available in the downloaded atlas were studied. These included the inferior and superior colliculi, which are paired nonsubcortical posterior structures, the inferior colliculus being the closest to the cerebellum, as well as the thalamus, an unpaired central structure, and the hemisphere as a whole. A two-sample unpaired *t*-test was performed to compare both strains (significant level at 5%).

Results

Comparison between atlas-based and manual segmentations

As an initial step, the MRI volume was registered to the block-face volume for the three steps of the registration process. The T1-weighted MRI and the derived atlas were registered in less than 30 min (tests realized with an Intel® Xeon® CPU 5150 at 2.66 GHz).

Fig. 3 shows, in three views, the superimposition of the contours of the T1-weighted MR image (in white) on one 3D-reconstructed histological volume from an APP/PS1 mouse before (Fig. 3A) and after each step of the registration strategy: rigid registration (Fig. 3B), affine registration (Fig. 3C), and elastic registration (Fig. 3D). Arrow 1 (focus on the external contours) between Figs. 3A and B shows that rigid transformation was able to center both images. Volume differences between atlas and experimental data were compensated for using the affine transformation (Arrow 1 between Figs. 3B and C). Finally, local differences between atlas and experimental data were greatly reduced thanks to the elastic transformation: in Fig. 3D, the external contours (1) and those defining inner structures such as the corpus callosum (2) and the hippocampus (3) are correctly superimposed. Deformation grids, Fig. 3E, show that external contours were more severely deformed by the nonlinear transformation than inner structures (dotted arrows).

Table 1 displays volume differences (Table 1A), Dice coefficients (Table 1B), and sensitivity (Table 1C) criteria computed for the cortex, corpus callosum, hippocampus, striatum, and substantia nigra of one PS1 and one APP/PS1 mouse before and after rigid, affine, and elastic registration. Globally, for each ROI, similar variations in criteria were observed for both mice. The greatest increase in Dice and sensitivity indices was observed after the rigid transformation (~170% on average for both mice) as illustrated by data centering in Fig. 3B. The scaling and shearing parameters of the affine transformation were able to improve most segmentation matching in space (mean gain of $\kappa \sim 0.5\%$ between rigid and affine registration steps) over Δ_V and Se scores (mean loss of Se $\sim 5\%$ and mean gain of $\Delta_V \sim 175\%$ between the two deformations). The 3×10^3 DOF of the elastic transformation were able to correct these losses and to optimize the overlapping criteria: between the last two steps, κ scores increased by ~7% and Se scores by ~9%, and Δ_V decreased by ~23%. The final Δ_V scores show that the atlas could measure, in 3D-reconstructed *post mortem* data, the volume of the cortex with a mean error of 6%, the one of the corpus
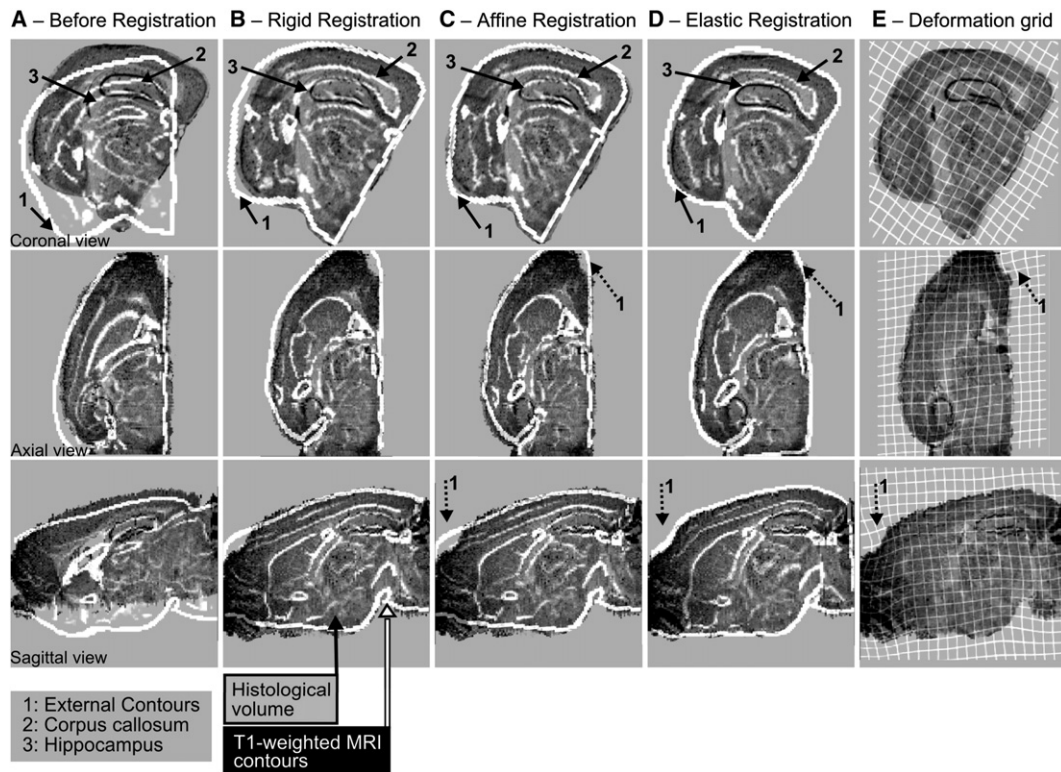
Fig. 3. Superimposition of the contours of the T1-weighted MR image (in white) on one APP/PS1 3D-reconstructed histological volume before (A) and after each step of the registration strategy: rigid registration (B), affine registration (C), and elastic registration (D). The corresponding block-face volume was used as the reference image for the registration process. The external contours (1) in B show that rigid transformation was able to center both images and that the affine transformation could then compensate for volume differences between the atlas and experimental data (C). With the external contours (1) and those defining inner structures such as the corpus callosum (2) and the hippocampus (3) correctly superimposed in D, the elastic transformation was able to locally adjust registration between MRI and experimental data. Deformation grids (E) show that the external contours were more severely deformed by nonlinear transformation than inner structures (dotted arrows).

Table 1

(A) Volume differences (Δ_V), (B) Dice coefficient (κ), and (C) Sensitivity (Se) computed for the cerebral cortex (Cx), corpus callosum (cc), hippocampus (Hc), striatum (Striat), and substantia nigra (SN) of one PS1 and one APP/PS1 mouse before (init) and after each step of the registration strategy (rigid, rig; affine, aff; and elastic, elast). Final mean scores ($\overline{\Delta_V} \sim 10\%, \overline{\kappa}$, and $\overline{Se} \geq 0.70$) show that this atlas accurately assigns voxels to the appropriate structure.

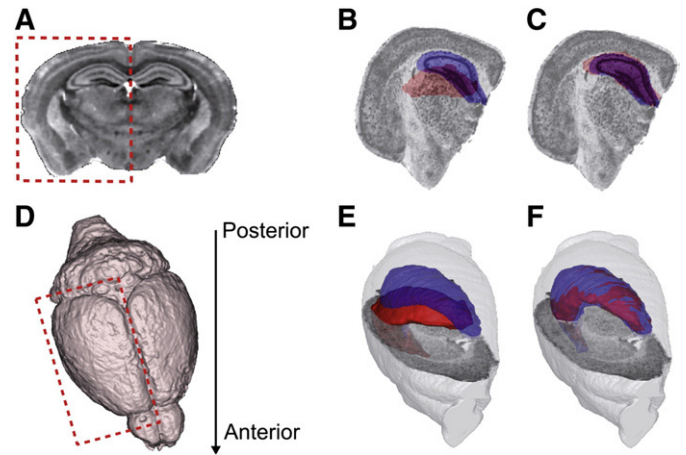|	PS1 mouse (ctrl)				APP/PS1 mouse (AD model)			
	Init	Rig	Aff	Elast	Init	Rig	Aff	Elast
(A) Volume differences (Δ_V)								
Cx	0.14	0.14	0.03	0.03	0.02	0.02	0.06	0.09
cc	0.12	0.12	0.28	0.29	0.01	0.02	0.10	0.08
Hc	0.08	0.08	0.24	0.18	0.19	0.19	0.27	0.15
Striat	0.06	0.06	0.23	0.08	0.06	0.06	0.14	0.05
SN	0.05	0.05	0.22	0.26	0.07	0.08	0.02	0.01
(B) Dice coefficient (κ)								
Cx	0.44	0.76	0.79	0.83	0.56	0.79	0.81	0.85
cc	0.08	0.42	0.48	0.54	0.09	0.41	0.42	0.58
Hc	0.38	0.82	0.79	0.83	0.41	0.82	0.82	0.86
Striat	0.45	0.80	0.81	0.83	0.47	0.79	0.81	0.81
SN	0.12	0.67	0.54	0.47	0.57	0.50	0.51	0.57
(C) Sensitivity (Se)								
Cx	0.48	0.82	0.78	0.82	0.57	0.80	0.78	0.82
cc	0.07	0.40	0.42	0.47	0.09	0.41	0.40	0.56
Hc	0.36	0.79	0.70	0.76	0.37	0.75	0.72	0.80
Striat	0.44	0.78	0.73	0.80	0.45	0.77	0.76	0.79
SN	0.11	0.65	0.49	0.41	0.59	0.52	0.50	0.57

Overlapping criteria computed for five ROIs of one PS1 and one APP/PS1 mouse before and after each step of the registration strategy.

Fig. 4. Superimposition of the atlas-based segmentation of the hippocampus (red) on the manual segmentation (blue) delineated within the histological volume of one APP/PS1 mouse brain, before and after registration of atlas to experimental data. The part (dashed rectangles) of the MRI and of the 3D digital atlas under study are shown in A and D, respectively. One histological section and the 3D-reconstructed histological volume are represented with the manually delineated hippocampus (blue) and the same hippocampus yielded by atlas-based segmentation (red): B (2D view) and E (3D view) display the superimposition of segmentations before registration; C (2D view) and F (3D view) display the superimposition of segmentations after registration. The figure shows a good match between the two types of segmentation after the registration process.

callosum with a mean error of 18%, the hippocampal volume with a mean error of 17%, striatal volume with a mean error of 6% and the volume of the substantia nigra with a mean error of 14%. High final κ and Se indices ($\overline{\kappa} \sim 0.72$ and $\overline{Se} \sim 0.68$) attest that this atlas properly assigned most of voxels to the appropriate structure. This atlas could thus be used to automatically identify structures within a 3D-reconstructed *post mortem* volume. A visual representation of atlas registration on one APP/PS1 experimental sample is shown in Fig. 4.

For easier understanding, the parts (dashed rectangles) of the MRI and of the 3D digital atlas under study are presented in Figs. 4A and D, respectively. One histological section and the 3D-reconstructed histological volume are represented with the manually delineated hippocampus (blue) and the same hippocampus yielded by atlas-based segmentation (red): Figs. 4B (2D view) and E (3D view) display the superimposition of segmentations before registration; Figs. 4C (2D view) and F (3D view) display the superimposition of segmentations after registration. The figure shows a good match between the two types of segmentation after the registration process. It also indicates that the mean error in hippocampal volume is distributed homogeneously throughout the ROI. Similar *a posteriori* qualitative inspections were carried out for all manually segmented ROIs (hippocampus, cortex, corpus callosum, striatum, and substantia nigra of both mice).

After verifying the reliability of our method against anatomical data, we assessed it against functional data by comparing mean activity in the ROI measured using atlas-based and manual segmentations (μ_{act}). Table 2 shows the $\mu_{act} \pm$ SD for the cerebral cortex, corpus callosum, hippocampus, striatum, and substantia nigra of one PS1 (Table 2A) and one APP/PS1 (Table 2B) mouse using both types of segmentation (where SD is the standard deviation of the mean for each type of segmentation). Variation coefficients (δ_μ) were computed and showed that differences between the μ_{act} of the two segmentation types were, on average, not significant ($\overline{\delta_\mu} \leq 5\%$). Except for the corpus callosum of the PS1 mouse, atlas-based segmentation provided a mean activity value for the ROIs equivalent to that estimated using manual segmentation.

Taken together, the results indicate that the proposed registration strategy is well adapted to match the downloaded atlas with our experimental data.

Registration of T1-weighted MRI with autoradiographic and histological volumes

The tests presented below were realized with one PS1 and one APP/PS1 mouse. As results were similar for the two mice, only those obtained with the APP/PS1 mouse are shown.

The T1-weighted MRI was entirely registered to the histological volume and then to the autoradiographic volume. The gray part of Table 3 presents overlapping criteria obtained after elastic registration, and standard deviations (SDs) are calculated to estimate differences between registrations using only the histological, autoradiographic or block-face volume as the reference image. Since most SDs were inferior or equal to 0.05, the measures between tests were not dispersed; results provided by all tests were thus equivalent.

We finally deformed the T1-weighted MRI by combining *post mortem* images to yield the reference one for the process. The white part of Table 3 shows the quantitative criteria computed for different combinations and the standard deviations (SDs) calculated between scores obtained by modifying the reference image. After rigid deformation, SD was below 0.05 for all criteria. We assumed that the reference image chosen for this step did not have any influence on registration quality; photography was chosen for the reasons cited previously. All affine registrations were then initialized with the rigid transformation estimated using the block-face volume as the reference image. SD was again inferior to 0.05 in all cases (except for the measure of sensitivity of the substantia nigra). Finally, after the elastic step, results remained close to each other. Thus, using combinations of reference images for registration did not lead to important differences in registration quality.

In accordance with the results mentioned earlier, the block-face volume was used as the reference image throughout the registration process. As the volumetric and functional measurements yielded by the registered atlas were validated using one PS1 and one APP/PS1 mouse (cf., Tables 1 and 2), the registration strategy was applied to the entire database.

Anatomofunctional data set analysis with atlas-based segmentation

We registered the T1-weighted MRI to each study subject using the same settings. Visual inspections, similar to those presented in Fig. 3, were carried out for the seven mice in this study. Once the MRI-based atlas was registered, we computed the average volume ($\overline{V} \pm$ SEM) and mean activity level ($\overline{\mu_{act}} \pm$ SEM) for several of the ROIs available in the atlas and for the hemisphere as a whole, for each strain (SEM standing for the standard error mean). The results presented in Table 4 show that for large regions (whole hemisphere and cortex), the atlas was able to precisely measure ROI volumes and activities. Atlas-based segmentation also provided accurate volumetric and activity measurements for subcortical structures (corpus callosum, hippocampus, striatum, and thalamus). For nonsubcortical ROIs (inferior and superior colliculi) and smaller and deeper structure (substantia nigra), volumetric measurements were more dispersed ($\overline{V}(\text{IC}_{PS1})) = 2.48 \pm 0.15$ mm^3, $\overline{V}(\text{SC}_{PS1}) = 6.12 \pm 0.42$ mm^3), as were activity measurements for the inferior colliculus ($\overline{\mu_{act}}(\text{IC}_{PS1}) = 233.11 \pm 16.55$ nCi/g, $\overline{\mu_{act}}(\text{IC}_{PS1/PS1}) = 295.80 \pm 26.98$ nCi/g) and substantia nigra ($\overline{\mu_{act}}(\text{SN}_{PS1}) = 177.08 \pm 20.98$ nCi/g). The *t*-test computed to compare strains revealed no statistically significant volumetric or functional differences between the groups at the level of the ROIs studied ($p \geq 0.05$).

Discussion

The main goal of this study was to develop a method capable of mapping a 3D digital atlas with our experimental 3D-reconstructed *post mortem* data sets, to automatically evaluate the volume and activity of mouse cerebral structures. The proposed approach used a downloaded 3D digital atlas based on MR images of wild-type mouse brains. The registration strategy developed, which gradually increased the degrees of freedom applied to the MRI to match *post mortem* volumes, allowed us to register images using a coarse-to-fine approach. The challenge faced by this study was to quantitatively evaluate the multimodal registration between data acquired *in situ* and *ex situ* (i.e., the atlas and experimental data, respectively) and to determine whether *ex situ* data could be analyzed using an atlas based on *in situ* imaging. Our method was successfully applied to a data set composed of three 3D brain imaging modalities for two transgenic strains.

Table 2
Comparison of mean ROI activity measured using manual ($\mu_{act(M)} \pm$ SD) and atlas-based segmentation ($\mu_{act(A)} \pm$ SD), with SD, the standard deviation measured within each type of segmentation. Measurements were carried out for the cerebral cortex (Cx), corpus callosum (cc), hippocampus (Hc), striatum (Striat), and substantia nigra (SN) of one PS1 (A) and one APP/PS1 (B) mouse after elastic registration. Variation coefficients (δ_μ) were computed for each ROI to estimate atlas segmentation error in comparison with measurements using manual segmentation. On average, the difference between the two measurements ($\overline{\delta_u} \leq 5\%$) is not significant. That shows that atlas-based segmentation yielded mean ROI activity values equivalent to those estimated by manual segmentation.

	μ_{act}(M) $\pm$ SD (nCi/g)	μ_{act}(A) $\pm$ SD (nCi/g)	δ_μ
(A) PS1 mouse (ctrl)			
Cx	265.38 ± 49.58	265.53 ± 48.36	< 0.01
cc	200.60 ± 38.70	226.82 ± 44.41	0.13
Hc	240.61 ± 40.49	239.31 ± 41.88	0.01
Striat	268.24 ± 37.75	273.21 ± 33.59	0.02
SN	221.61 ± 33.38	209.95 ± 35.30	0.05
(B) APP/PS1 mouse (AD model)			
Cx	275.96 ± 61.22	279.37 ± 57.61	0.01
cc	201.44 ± 48.01	208.30 ± 47.63	0.03
Hc	225.88 ± 38.66	225.52 ± 40.06	< 0.01
Striat	264.53 ± 48.95	276.19 ± 40.87	0.04
SN	187.37 ± 29.07	179.92 ± 26.16	0.04

Comparison of mean ROI activity measured for one PS1 (A) and one APP/PS1 (B) using manual and atlas-based segmentation.

Segmentation of 3D-reconstructed post mortem data using an MRI-based atlas

Manually creating a 3D atlas from *post mortem* images constitutes a huge amount of work. Manual segmentation must be carried out by experts on a large number of brain sections, a time-consuming approach. Thus, neuroscientists often cannot afford an exhaustive analysis of their *post mortem* data and choose to delineate only a few selected structures, whereas an investigation of the whole brain might be more informative.

Certain reports in the literature describe algorithms capable of generating a semiautomatic mouse brain segmentation based on MRI (Ali et al., 2005; Ma et al., 2005; Sharief et al., 2008; Scheenstra et al., 2009). These atlases have been preferentially used instead of those reconstructed from digital 2D atlas diagrams (Hjornevik et al., 2007; Purger et al., 2009) because of their improved 3D spatial coherence (Yelnik et al., 2007). The adaptation of these algorithms to *post mortem* data is not a trivial task, especially in light of the size of the data (e.g., the downloaded MRI (whole brain) size was 256×256×512 voxels with an isotropic resolution of 43 μm and the 3D-reconstructed histological volume (hemibrain) size was 479×420×120 voxels with a resolution of 21×21×80 μm^3). Moreover, these algorithms are capable of segmenting MR images thanks to the tissue contrast revealed by this kind of imaging modality that is different from tissue contrast revealed by *post mortem* images.

We chose to adapt an existing MRI-based 3D atlas to our biological data to bypass these difficulties. The atlas chosen was previously successfully used to characterize the morphometry of C57Bl/6J mouse brains (Badea et al., 2007) and to carry out a morphometric comparison between different genotypes: C57Bl6/J(B6), DBA/2J (D2), and nine recombinant inbred BXD strains (Badea et al., 2009). In these studies, the mice were approximately 9 weeks old. In our study, we developed and validated an original strategy for *in situ* and *ex situ* data registration in which the animals involved were of different ages.

Choice of reference image for the registration process

The proposed registration strategy used a three-step approach (rigid, affine, and elastic transformation) to permit the registration of data with different resolutions and sizes. The block-face volume was first chosen as the reference image because of its higher spatial coherence in comparison to the other imaging modalities and its similarity to MRI. Registrations were also realized using only histological or autoradiographic volumes or a combination of imaging modalities throughout the process. As this did not improve the quality of registration (cf., Table 3), we subsequently registered MR images to the block-face volume only.

Evaluation of registration

It is a challenge to obtain perfect data superimposition and maximal overlapping scores (minimal volume differences) using multimodal registration, since the information contained in one image is not necessarily present in the other. Additional difficulties surfaced in this study because we registered cropped whole-brain MR images to *post mortem* hemibrain images and compared segmentation based on images acquired inside (atlas) and outside the skull (anatomical data set). Indeed, physical deformations did result from the experimental procedure: our samples being sections of hemibrains (excluding the olfactory bulb and cerebellum) cut on a cryostat and mounted on glass slides, cerebral tissues could have been deformed due to handling. Another consequence of registration using *in situ* (intracranial MR images) and *ex situ* (experimental data) images was the loss of the meninges and the cerebrospinal fluid in the latter, whereas the former were better preserved. Some ROIs, such as the ventricles, thus no longer appeared similar in the two images. Neighboring structures, like the hippocampus and corpus callosum in our study, could

Table 3
(A) Volume differences (Δ_V), (B) Dice coefficient (κ), and (C) Sensitivity (Se) computed for the cerebral cortex (Cx), corpus callosum (cc), hippocampus (Hc), striatum (Striat), and substantia nigra (SN) of one APP/PS1 mouse using successively the histological (His), autoradiographic (Aut), or block-face (Ph) volume as the reference image for each of three registration steps (Rig, Aff, and Elast) (white part) and for the entire registration process (gray part). White part: for each registration step, standard deviations (SDs) were calculated between scores following changes in the reference image. As globally measures were not dispersed (SD ≤ 0.05), Ph volume was chosen as the reference image for this step and the subsequent registration was initialized with transformation(s) estimated using Ph as the reference image. Gray part: SDs computed between scores also show that there was no important difference between the three reference images assessed.

Ref			Cx		cc		Hc		Striat		SN	
Rig	Aff	Elast	Score	SD	Score	SD	Score	SD	Score	SD	Score	SD
(A) Volume differences Δ_V												
His			0.02		0.01		0.19		0.06		0.05	
Aut			0.02	< 0.01	0.01	< 0.01	0.19	< 0.01	0.06	< 0.01	0.07	0.01
Ph			0.02		0.02		0.19		0.06		0.08	
Ph	His		< 0.01		0.03		0.21		0.07		0.06	
Ph	Aut		0.02	0.03	0.01	0.05	0.19	0.04	0.06	0.05	0.06	0.02
Ph	Ph		0.06		0.10		0.27		0.14		0.02	
Ph	Ph	His	< 0.01		0.08		0.07		0.19		0.08	
Ph	Ph	Aut	0.04	0.04	0.11	0.02	0.03	0.07	0.16	0.07	0.08	0.04
Ph	Ph	Ph	0.09		0.08		0.15		0.05		0.01	
His	His	His	0.02		0.08		0.04		0.19		0.10	
Aut	Aut	Aut	0.05	0.04	0.09	0.01	0.06	0.06	0.16	0.07	0.11	0.05
Ph	Ph	Ph	0.09		0.08		0.15		0.05		0.01	
(B) Dice coefficient κ												
His			0.79		0.38		0.81		0.78		0.48	
Aut			0.79	< 0.01	0.41	0.02	0.83	0.01	0.78	< 0.01	0.43	0.04
Ph			0.79		0.41		0.82		0.79		0.50	
Ph	His		0.82		0.50		0.85		0.83		0.59	
Ph	Aut		0.82	0.01	0.48	0.04	0.85	0.02	0.82	0.01	0.60	0.05
Ph	Ph		0.81		0.42		0.82		0.81		0.51	
Ph	Ph	His	0.84		0.56		0.89		0.78		0.66	
Ph	Ph	Aut	0.84	0.01	0.58	0.01	0.90	0.02	0.78	0.02	0.67	0.06
Ph	Ph	Ph	0.85		0.58		0.86		0.81		0.57	
His	His	His	0.84		0.57		0.89		0.79		0.65	
Aut	Aut	Aut	0.84	0.01	0.59	0.01	0.89	0.02	0.79	0.01	0.67	0.06
Ph	Ph	Ph	0.85		0.58		0.86		0.81		0.57	
(C) Sensitivity (Se)												
His			0.80		0.38		0.74		0.76		0.49	
Aut			0.80	< 0.01	0.40	0.02	0.76	0.01	0.76	< 0.01	0.45	0.04
Ph			0.80		0.41		0.75		0.77		0.52	
Ph	His		0.82		0.49		0.77		0.80		0.60	
Ph	Aut		0.83	0.03	0.48	0.05	0.78	0.03	0.79	0.02	0.62	0.06
Ph	Ph		0.78		0.40		0.72		0.76		0.50	
Ph	Ph	His	0.84		0.58		0.86		0.86		0.68	
Ph	Ph	Aut	0.85	0.02	0.62	0.03	0.88	0.05	0.85	0.04	0.69	0.07
Ph	Ph	Ph	0.82		0.56		0.80		0.79		0.57	
His	His	His	0.85		0.60		0.87		0.87		0.69	
Aut	Aut	Aut	0.86	0.02	0.62	0.03	0.87	0.04	0.86	0.04	0.70	0.07
Ph	Ph	Ph	0.82		0.56		0.80		0.79		0.57	

Choice of reference image for the MRI registration process.

have been misregistered as a consequence of ventricular deformation. This could explain the final difference in hippocampal volume, Dice coefficient and sensitivity of the corpus callosum presented in Table 1. Segmentation errors could also have occurred due to the definition of ROIs, a problem that arose when we compared two different segmentation methods. Indeed, although compromises were made between post-processed atlas-based segmentation and manual delineation to compare similar structures as far as possible (e.g., by merging the ROIs nucleus accumbens and caudate putamen to yield the striatum), intrinsic differences in definition remained. These differences were particularly obvious in thin structures such as the corpus callosum or complex structures such as the hippocampus, which has the shape of a ram's horn (cf., Fig. 4). The registration of these structures could have been problematic during scaling adjustments, since the proposed strategy followed a global approach and the registration was mainly driven by large and noncomplex ROIs at the expense of small and complex ROIs introducing a weighted contribution of the different structures to the final registration estimated. A small registration error in a leading ROI could

have led to important volumetric and functional variations in a smaller adjacent structure.

Registration volumes were qualitatively and quantitatively evaluated. The superimposition of the contours of the MRI on the 3D histological volume as well as the superimposition of atlas-based and manual segmentations showed that MR images and the derived atlas could be progressively deformed to match *post mortem* data (cf., Figs. 3 and 4). The grids presented in Fig. 3 demonstrate that the nonlinear transformation did not result in excessive deformation of inner structures. Table 1 summarizes overlapping criteria (volume differences, Dice coefficient, and sensitivity index) for the cortex, corpus callosum, hippocampus, striatum, and substantia nigra, computed at each registration step to quantitatively evaluate, according to size and location, the accuracy of the match between atlas-based segmentation and the manual delineation that served as the reference. Previous visual assessments and the high scores obtained after the affine step demonstrate that the elastic registration was well initialized and that the FFD algorithm could efficiently

Table 4

Average volume ($\overline{V} \pm$ SEM) and mean activity ($\overline{\mu_{act}} \pm$SEM) were computed after elastic registration for the whole hemisphere (Hemisphere), cerebral cortex (Cx), corpus callosum (cc), hippocampus (Hc), inferior colliculus (IC), superior colliculus (SC), striatum (Striat), substantia nigra (SN), and thalamus (Thal). SEM represents the standard error mean calculated for each group. Analysis of large (Hemisphere, Cx) and subcortical structures (cc, Hc, Striat, Thal) provided homogeneous measurements within strains, whereas measurements for smaller nonsubcortical ROIs (IC, SC, and SN) were more dispersed. The present results did not reveal statistically significant volumetric or functional differences between groups on the scale of the ROIs ($p \geq 0.05$).

	PS1 mice ($n = 3$)	APP/PS1 mice ($n = 4$)
(A) Volume $\overline{V} \pm$ SEM (mm³)		
Hemisphere	176.77 ± 8.19	175.57 ± 1.96
Cx	75.64 ± 4.21	75.28 ± 0.65
cc	5.84 ± 0.24	5.98 ± 0.03
Hc	11.89 ± 0.32	12.90 ± 0.24
IC	2.48 ± 0.15	2.49 ± 0.12
SC	6.12 ± 0.42	5.55 ± 0.05
Striat	12.53 ± 0.16	12.58 ± 0.25
SN	0.75 ± 0.02	0.79 ± 0.04
Thal	17.27 ± 0.76	16.49 ± 0.75
(B) Activity $\overline{\mu_{act}} \pm$ SEM (nCi/g)		
Hemisphere	216.04 ± 3.12	222.51 ± 1.72
Cx	270.54 ± 2.68	272.68 ± 2.39
cc	211.45 ± 7.87	215.00 ± 3.17
Hc	237.67 ± 1.08	228.24 ± 3.39
IC	233.11 ± 16.55	295.80 ± 26.98
SC	252.78 ± 6.97	258.68 ± 6.51
Striat	284.04 ± 5.55	274.30 ± 0.87
SN	177.08 ± 20.98	188.22 ± 9.02
Thal	263.76 ± 5.42	242.96 ± 1.78

Volumetric (A) and functional (B) analysis of brain structures for PS1 and APP/PS1 mice.

optimize registration with a $10 \times 10 \times 10$ matrix of control points. A pyramidal approach at this step was thus not necessary, allowing us to reduce computation time.

High final overlapping scores ($\overline{\kappa} \sim 0.72$ and $\overline{Se} \sim 0.68$) attest that the MRI-based atlas properly assigned most of voxels to the appropriate anatomical structure. Figs. 4C and F show that the volume differences calculated between the two types of segmentations were homogeneously distributed throughout the structure; the general shape of the ROI was preserved. The atlas could thus be used to automatically identify structures within a 3D-reconstructed *post mortem* volume. This conclusion was confirmed by most coefficients of variation of mean ROI activity measured using atlas-based and manual segmentation that were not significant ($\overline{\delta_u} \leq 5\%$ presented in Table 2). Indeed, atlas-based segmentation yielded a mean ROI activity equivalent to that yielded by manual segmentation. An anatomofunctional analysis of our data set with this MRI-based atlas was thus carried out.

Use of an MRI-based atlas to analyze an anatomofunctional data set

The atlas was registered to all the subjects in the database, and average volume and mean activity level were computed for several ROIs. Results presented in Table 4 show globally homogeneous measurements within each group (e.g., $\overline{V}(Hc_{APP/PS1}) = 12.9 \pm 0.24$ mm³), which agree with the values yielded by another digital atlas registered to *in vivo* data from whole mouse brains and presented in Maheswaran et al. (2009b) ($\overline{V}(Hc_{TASTPM}) = 25.4 \pm 0.75$ mm³). The work described in Delatour et al. (2006) deals with the same transgenic animals as those used in our study. The gap between their results and our volumetric measurements of the hippocampus, shown in Table 4, could be explained by the different methods used. To estimate volumes, they used the Cavalieri method on 40-μm-thick serial coronal sections, analyzing only one out of every eight sections.

More dispersed measurements in our study, such as $\overline{\mu_{act}}(_{APP/PS1}) = 295.80 \pm 26.98$ nCi/g and $\overline{\mu_{act}}(_{PS1}) = 177.08 \pm 20.98$, could be due to the size and location of the ROI studied: the inferior colliculus is a nonsubcortical structure located close to the cerebellum and the substantia nigra is a subthalamic structure nonprotected by the cortical shell. They could have been deformed during brain extraction and cutting. In addition, as there are small structures ($\overline{V}(IC) \sim 2.49$ mm³, $\overline{V}(SN) \sim 0.77$ mm³), a slight misregistration of adjacent structures (such as the superior colliculus or more likely the cortex for the inferior colliculus or the thalamus for the substantia nigra) could have led to a more substantial misregistration of these ROIs. The registered atlas would, therefore, have measured in part the activity of adjacent structures. This result illustrates a drawback of the use of an atlas to analyze autoradiographic data.

According to Table 4, neither functional nor volumetric differences between groups on the scale of the ROIs were statistically significant, which agrees with previous studies carried out on the whole brain (Sadowski et al., 2004; Delatour et al., 2006). These results indicate that, even with the additional deformation due to splitting of the brains and probable misregistration, as mentioned above, our automated *post mortem* data analysis method using MRI-based atlas registration provided results with a similar reproducibility and accuracy to those of more standard methods. Sadowski et al. (2004) have nevertheless observed statistically significant differences between substructures of the hippocampus. This suggests that our analysis is dependent on the scale of segmentation.

Conclusion

The present study indicates that our methodology led to the successful coregistration of MRI data from young wild type mice with 3D-reconstructed *post mortem* brains of older animals from two different transgenic strains. The MRI-based atlas fit our study well and could also be used as a template for fully automated mouse brain segmentation. Whereas standard approaches are based on manual analysis and thus limit the study to a few regions or tissue sections, this method is easier, faster, and more objective, since it is non-operator-dependent, and directly provides volumetric and functional information for several brain structures in all sections considered. As described in Dauguet et al. (2009), the use of the block-face volume to reconstruct and align histological or autoradiographic data with the MRI-based atlas permits biologists to study several ROIs in selected sections or to focus their work on entire structures. This is a promising approach for the investigation of a large number of *post mortem* data sets on the scale of individual structures and could find several applications in exploratory studies in the neurosciences.

Other investigative methods could also be improved by the use of this registered atlas. The voxel-wise analysis (approach called without *a priori*) of *post mortem* rodent brain images reveals differences at the substructure level, and thus provides more detailed biological results. However, this kind of analysis often suffers from the large amount of voxels to be computed. Combining registered atlas segmentation with voxel-wise analysis could limit statistical tests to selected voxels and subsequently allow the correction of statistical tests and the refinement of results (Genovese et al., 2002; Dubois et al., 2008b).

Finally, another advantage of registering *ex situ* and *in situ* data could be the improvement of *in vivo*–*post mortem* registration. This approach could indeed be used to guide *in vivo* PET scan analysis, and the results could subsequently be compared with activity revealed by autoradiography.

Acknowledgments

References

Ali, A.A., Dale, A.M., Badea, A., Johnson, G.A., 2005. Automated segmentation of neuroanatomical structures in multispectral MR microscopy of the mouse brain. Neuroimage 27 (2), 425–435.

Badea, A., Ali-Sharief, A.A., Johnson, G.A., 2007. Morphometric analysis of the C57BL/6J mouse brain. Neuroimage 37 (3), 683–693. Sep http://dx.doi.org/10.1016/j.neuroimage.2007.05.046.

Badea, A., Johnson, G.A., Williams, R.W., 2009. Genetic dissection of the mouse brain using high-field magnetic resonance microscopy. Neuroimage 45 (4), 1067–1079. May http://dx.doi.org/10.1016/j.neuroimage.2009.01.021.

Blanchard, V., Moussaoui, S., Czech, C., Touchet, N., Bonici, B., Planche, M., Canton, T., Jedidi, I., Gohin, M., Wirths, O., Bayer, T.A., Langui, D., Duyckaerts, C., Tremp, G., Pradier, L., 2003. Time sequence of maturation of dystrophic neurites associated with abeta deposits in APP/PS1 transgenic mice. Exp. Neurol. 184 (1), 247–263. Nov.

Bock, N.A., Kovacevic, N., Lipina, T.V., Roder, J.C., Ackerman, S.L., Henkelman, R.M., 2006. *In vivo* magnetic resonance imaging and semiautomated image analysis extend the brain phenotype for *cdf/cdf* mice. J. Neurosci. 26 (17), 4455–4459.

Boline, J., Lee, E.-F., Toga, A.W., 2008. Digital atlases as a framework for data sharing. Front Neurosci. 2 (1), 100–106. Jul http://dx.doi.org/10.3389/neuro.01.012.2008.

Chakravarty, M.M., Bertrand, G., Hodge, C.P., Sadikot, A.F., Collins, D.L., 2006. The creation of a brain atlas for image guided neurosurgery using serial histological data. Neuroimage 30 (2), 359–376. Apr http://dx.doi.org/10.1016/j.neuroimage.2005.09.041.

Dauguet, J., Delzescaux, T., Condé, F., Mangin, J.-F., Ayache, N., Hantraye, P., Frouin, V., 2007. Three-dimensional reconstruction of stained histological slices and 3D non-linear registration with in-vivo MRI for whole baboon brain. J. Neurosci. Methods 164 (1), 191–204.

Dauguet, J., Cond, F., Hantraye, P., Frouin, V., Delzescaux, T., 2009. Generation of a 3D atlas of the nuclear division of the thalamus based on histological sections of primate: intra- and intersubjet atlas-to-MRI warping. IRBM 30, 281–291.

Delatour, B., Gugan, M., Volk, A., Dhenain, M., 2006. *In vivo* MRI and histological evaluation of brain atrophy in APP/PS1 transgenic mice. Neurobiol. Aging 27 (6), 835–847 Jun http://dx.doi.org/10.1016/j.neurobiolaging.2005.04.011.

Deriche, R., 1987. Separable recursive filtering for efficient multi-scale edge detection. Proceeding International Workshop on Machine Vision and Machine Intelligence, pp. 18–23. Feb. 2-5. Tokyo.

Dhenain, M., Ruffins, S.W., Jacobs, R.E., 2001. Three-dimensional digital mouse atlas using high-resolution MRI. Dev. Biol. 232 (2), 458–470. Apr http://dx.doi.org/10.1006/dbio.2001.0189.

Dice, L., 1945. Measures of the amount of ecologic association between species. Ecology 26 (3), 297–302. Jul.

Dorr, A.E., Lerch, J.P., Spring, S., Kabani, N., Henkelman, R.M., 2008. High resolution three-dimensional brain atlas using an average magnetic resonance image of 40 adult C57Bl/6J mice. Neuroimage 42 (1), 60–69. Aug http://dx.doi.org/10.1016/j.neuroimage.2008.03.037.

Dubois, A., Dauguet, J., Souedet, N., Herard, A.-S., Riviere, D., Cointepas, Y., Bonvento, G., Hantraye, P., Frouin, V., Delzescaux, T., 2008a. BrainRAT: Brain Reconstruction and Analysis Toolbox. A freely available toolbox for the 3D reconstruction of anatomo-functional brain sections in rodents. The 38th annual meeting of the Society for Neuroscience, Washington, USA.

Dubois, A., Herard, A.-S., Flandin, G., Duchesnay, E., Besret, L., Frouin, V., Hantraye, P., Bonvento, G., Delzescaux, T., 2008b. Quantitative validation of voxel-wise statistical analyses of autoradiographic rat brain volumes: application to unilateral visual stimulation. Neuroimage 40 (2), 482–494. Apr.

Genovese, C.R., Lazar, N.A., Nichols, T., 2002. Thresholding of statistical maps in functional neuroimaging using the false discovery rate. Neuroimage 15 (4), 870–878. Apr http://dx.doi.org/10.1006/nimg.2001.1037.

Herard, A.S., Dubois, A., Escartin, C., Tanaka, K., Delzescaux, T., Hantraye, P., Bonvento, G., 2005. Decreased metabolic response to visual stimulation in the superior colliculus of mice lacking the glial glutamate transporter glt-1. Eur. J. NeuroSci. 22(d), 1807–1811.

Hjornevik, T., Leergaard, T.B., Darine, D., Moldestad, O., Dale, A.M., Willoch, F., Bjaalie, J.G., 2007. Three-dimensional atlas system for mouse and rat brain imaging data. Front Neuroinform. 1, 4. http://dx.doi.org/10.3389/neuro.11.004.2007.

Johnson, G.A., Ali-Sharief, A., Badea, A., Brandenburg, J., Cofer, G., Fubara, B., Gewalt, S., Hedlund, L.W., Upchurch, L., 2007. High-throughput morphologic phenotyping of the mouse brain with magnetic resonance histology. Neuroimage 37 (1), 82–89. Aug http://dx.doi.org/10.1016/j.neuroimage.2007.05.013.

Li, X., Yankeelov, T.E., Rosen, G.D., Gore, J.C., Dawant, B.M., 2009. Enhancement of histological volumes through averaging and their use for the analysis of magnetic resonance images. Magn. Reson. Imaging 27 (3), 401–416. Apr http://dx.doi.org/10.1016/j.mri.2008.07.016.

Ma, Y., Hof, P.R., Grant, S.C., Blackband, S.J., Bennett, R., Slatest, L., McGuigan, M.D., Benveniste, H., 2005. A three-dimensional digital atlas database of the adult C57BL/6J mouse brain by magnetic resonance microscopy. Neuroscience 135 (4), 1203–1215.

Ma, Y., Smith, D., Hof, P.R., Foerster, B., Hamilton, S., Blackband, S.J., Yu, M., Benveniste, H., 2008. *In Vivo* 3D digital atlas database of the adult C57BL/6J mouse brain by magnetic resonance microscopy. Front Neuroanat. 2, 1. http://dx.doi.org/10.3389/neuro.05.001.2008.

Mackenzie-Graham, A., Lee, E.-F., Dinov, I.D., Bota, M., Shattuck, D.W., Ruffins, S., Yuan, H., Konstantinidis, F., Pitiot, A., Ding, Y., Hu, G., Jacobs, R.E., Toga, A.W., 2004. A multimodal, multidimensional atlas of the C57BL/6J mouse brain. J. Anat. 204 (2), 93–102.

Maes, F., Collignon, A., Vandermeulen, D., Marchal, G., Suetens, P., 1997. Multimodality image registration by maximization of mutual information. IEEE Trans. Med. Imaging 16 (2), 187–198.

Maheswaran, S., Barjat, H., Bate, S.T., Aljabar, P., Hill, D.L.G., Tilling, L., Upton, N., James, M.F., Hajnal, J.V., Rueckert, D., 2009a. Analysis of serial magnetic resonance images of mouse brains using image registration. Neuroimage 44 (3), 692–700. Feb http://dx.doi.org/10.1016/j.neuroimage.2008.10.016.

Maheswaran, S., Barjat, H., Rueckert, D., Bate, S.T., Howlett, D.R., Tilling, L., Smart, S.C., Pohlmann, A., Richardson, J.C., Hartkens, T., Hill, D.L.G., Upton, N., Hajnal, J.V., James, M.F., 2009b. Longitudinal regional brain volume changes quantified in normal aging and Alzheimer's APP/PS1 mice using MRI. Brain Res. 1270, 19–32. May http://dx.doi.org/10.1016/j.brainres.2009.02.045.

Malandain, G., Bardinet, E., Nelissen, K., Vanduffel, W., 2004. Fusion of autoradiographs with an MR volume using 2-D and 3-D linear transformations. NeuroImage 23 (1), 111–127.

Mattes, D., Haynor, D., Vesselle, H., Lewellen, T., Eubank, W., 2003. PET–CT image registration in the chest using free-form deformations. IEEE Trans. Med. Imaging 22.

Nguyen, P., Holschneider, D., Maarek, J., Yang, J., Mandelkern, M., 2004. Statistical parametric mapping applied to an autoradiographic study of cerebral activation during treadmill walking in rats. NeuroImage 23 (1), 252–259.

Ourselin, S., Roche, A., Subsol, G., Pennec, X., Ayache, N., 2001. Reconstructing a 3D structure from serial histological sections. Image Vis. Comp. 19 (1–2), 25–31.

Paxinos, G., Franklin, K., 2001. The Mouse Brain in Stereotaxic Coordinates. Academic Press, San Diego, CA.

Prima, S., Ourselin, S., Ayache, N., 2002. Computation of the mid-sagittal plane in 3D brain images. IEEE Trans. Med. Imaging 21 (2), 122–138.

Purger, D., McNutt, T., Achanta, P., Quiones-Hinojosa, A., Wong, J., Ford, E., 2009. A histology-based atlas of the C57BL/6J mouse brain deformably registered to *in vivo* MRI for localized radiation and surgical targeting. Phys. Med. Biol. 54 (24), 7315–7327. Nov http://dx.doi.org/10.1088/0031-9155/54/24/005.

Rueckert, D., Sonoda, L.I., Hayes, C., Hill, D.L., Leach, M.O., Hawkes, D.J., 1999. Nonrigid registration using free-form deformations: application to breast MR images. IEEE Trans. Med. Imaging 18 (8), 712–721.

Sadowski, M., Pankiewicz, J., Scholtzova, H., Ji, Y., Quartermain, D., Jensen, C.H., Duff, K., Nixon, R.A., Gruen, R.J., Wisniewski, T., 2004. Amyloid-beta deposition is associated with decreased hippocampal glucose metabolism and spatial memory impairment in APP/PS1 mice. J. Neuropathol. Exp. Neurol. 63 (5), 418–428. May.

Scheenstra, A.E.H., van de Ven, R.C.G., van der Weerd, L., van den Maagdenberg, A.M.J.M., Dijkstra, J., Reiber, J.H.C., 2009. Automated segmentation of *in vivo* and *ex vivo* mouse brain magnetic resonance images. Mol. Imaging 8 (1), 35–44.

Schormann, T., Dabringhaus, A., Zilles, K., 1995. Statistics of deformations in histology and application to improved alignment with MRI. IEEE Trans. Med. Imaging 14, 25–35.

Sharief, A.A., Badea, A., Dale, A.M., Johnson, G.A., 2008. Automated segmentation of the actively stained mouse brain using multi-spectral mr microscopy. Neuroimage 39 (1), 136–145. Jan http://dx.doi.org/10.1016/j.neuroimage.2007.08.028.

Swanson, L., 1998. Brain maps: structure of the rat brain, 2nd Revised Ed., Elsevier Science, Amsterdam.

Valla, J., Schneider, L., Reiman, E.M., 2006. Age- and transgene-related changes in regional cerebral metabolism in PSAPP mice. Brain Res. 1116 (1), 194–200. Oct http://dx.doi.org/10.1016/j.brainres.2006.07.097.

Viola, P., Wells, W.M., 1997. Alignment by maximization of mutual information. Int. J. Comp. Vis. 24, 137–154.

Wong, P.C., Cai, H., Borchelt, D.R., Price, D.L., 2002. Genetically engineered mouse models of neurodegenerative diseases. Nat. Neurosci. 5 (7), 633–639. Jul http://dx.doi.org/10.1038/nn0702-633.

Yelnik, J., Bardinet, E., Dormont, D., Malandain, G., Ourselin, S., Tandé, D., Karachi, C., Ayache, N., Cornu, P., Agid, Y., 2007. A three-dimensional, histological and deformable atlas of the human basal ganglia: I. Atlas construction based on immunohistochemical and MRI data. Neuroimage 34 (2), 618–638.

Zijdenbos, A.P., Dawant, B.M., Margolin, R.A., Palmer, A.C., 1994. Morphometric analysis of white matter lesions in MR images: method and validation. IEEE Trans. Med. Imaging 13 (4), 716–724. http://dx.doi.org/10.1109/42.363096.